Hyperspectral reflectance measurements from UAS under intermittent clouds: Correcting irradiance measurements for sensor tilt

Christian J. Köppl [a],[*], Radu Malureanu [b], Carsten Dam-Hansen [b], Sheng Wang [a], Hongxiao Jin [a], Stefano Barchiesi [c], Juan M. Serrano Sandí [d], Rafael Muñoz-Carpena [e], Mark Johnson [f], Ana M. Durán-Quesada [g], Peter Bauer-Gottwein [a], Ursula S. McKnight [a], Monica Garcia [a]

[a] Department of Environmental Engineering, Technical University of Denmark, Bygningstorvet, Bygning 115, 2800 Kgs. Lyngby, Denmark
[b] Department of Photonics Engineering, Technical University of Denmark, Ørsteds Plads, building 343, 2800 Kgs. Lyngby, Denmark
[c] School of Natural Resources and Environment, University of Florida, 103 Black Hall, Gainesville, FL 32611, USA
[d] Palo Verde Research Station, Organization for Tropical Studies, Parque Nacional Palo Verde, Bagaces 50401, Costa Rica
[e] Agricultural and Biological Engineering, University of Florida, 1741 Museum Road, Gainesville, FL 32611, USA
[f] Department of Earth, Ocean and Atmospheric Sciences, University of British Columbia, 2020 – 2207 Main Mall, Vancouver V6T 1Z4, BC, Canada
[g] Atmospheric, Oceanic and Planetary Physics Department & Climate System Observation Laboratory, School of Physics, University of Costa Rica, San José, San Pedro, Costa Rica

ARTICLE INFO

ABSTRACT

One great advantage of optical hyperspectral remote sensing from unmanned aerial systems (UAS) compared to satellite missions is the possibility to fly and collect data below clouds. The most typical scenario is flying below intermittent clouds and under turbulent conditions, which causes tilting of the platform. This study aims to advance hyperspectral imaging from UAS in most weather conditions by addressing two challenges: (i) the radiometric and spectral calibrations of miniaturized hyperspectral sensors; and (ii) tilting effects on measured downwelling irradiance. We developed a novel method to correct the downwelling irradiance data for tilting effects. It uses a hybrid approach of minimizing measured irradiance variations for constant irradiance periods and spectral unmixing, to calculate the spectral diffuse irradiance fraction for all irradiance measurements within a flight. It only requires the platform's attitude data and a standard incoming light sensor. We demonstrated the method at the Palo Verde National Park wetlands in Costa Rica, a highly biodiverse area. Our results showed that the downwelling irradiance correction method reduced systematic shifts caused by a change in flight direction of the UAS, by 87% and achieving a deviation of 2.78% relative to a on ground reference in terms of broadband irradiance. High frequency (< 3 s) irradiance variations caused by high-frequency tilting movements of the UAS were reduced by up to 71%. Our complete spectral and radiometric calibration and irradiance correction can significantly remove typical striped illumination artifacts in the surface reflectance-factor map product. The possibility of collecting precise hyperspectral reflectance-factor data from UAS under varying cloud cover makes it more operational for environmental monitoring or precision agriculture applications, being an important step in advancing hyperspectral imaging from UAS.

1. Introduction

Hyperspectral imaging from satellites is a well-established tool, which is used to collect data worldwide and over large areas, but the pixel size of hyperspectral missions such as PRISMA or DESIS is tens of meters (Coppo et al., 2020). This resolution is not high enough to investigate small inland water bodies such as narrow streams, or to study vegetation traits or function at the individual scale. Furthermore, as

clouds are not transparent to radiation in the solar range, satellites or airplanes flying above the cloud base (typically around 2 km) cannot collect surface reflectance-factor data under overcast conditions. This leads to data gaps, with challenges in imputing the missing data, as both the scattering (BRDF) (Ishihara et al., 2015) and absorption properties of the land surface change under dominant diffuse or direct radiation conditions (Wang et al., 2019b).

The recent development of light-weight and miniaturized

---

* Corresponding author.
E-mail address: chkop@env.dtu.dk (C.J. Köppl).

hyperspectral sensors together with the advent of low-cost and reliable Unmanned Aerial Systems (UAS) is making hyperspectral applications more accessible, especially in the fields of environmental assessment and precision agriculture (Aasen et al., 2018), overcoming the limitations of satellites. Compared to studies using multispectral data, there are fewer studies using hyperspectral snapshot imagers on board of UAS, mostly on precision agriculture (Zarco-Tejada et al., 2013; Liu et al., 2017), species mapping (Huang et al., 2017; Cao et al., 2018) or detection of tree dieback (Honkavaara et al., 2020).

The main challenge for advancing UAS borne hyperspectral sensing towards operational applications is the improvement in the accuracy and consistency of the surface reflectance-factor datasets across space and time, acquired under a range of sky conditions including passing or intermittent clouds. The miniaturized sensors onboard UAS tend to have a lower signal-to-noise ratio (SNR) compared to larger instruments onboard of airplanes or satellites compromising the accuracy of surface radiance (Aasen et al., 2018; Manfreda et al., 2018; Zarco-Tejada et al., 2019). To address this it is necessary to develop workflows for accurate radiometric and spectral calibrations. Some studies have focused exclusively either on radiometric calibration (Aasen et al., 2014), or on spectral calibrations of few (Lucieer et al., 2014) or all spectral bands (Hakala et al., 2018) but to our knowledge, not both.

Another particularity of UAS, compared to airborne missions, is that they fly in the lower part of the atmospheric boundary layer (ABL), and they are much lighter, experiencing larger turbulence effects due to wind gusts (Finnigan et al., 2009; Suomi et al., 2015). The eddies create high frequency (< 3 s) movements in the platform orientation and affecting the fixed sensors' viewing geometry. Another source of systematic attitude changes in multirotor UAS platforms is due to changes in flight direction, where the UAS has to tilt forward, in order to propel itself. These attitude variations lead to variations in fixed sensor's viewing angle (SVA). For instance, in the case of incoming light sensors (ILS), departures in the SVA of less than $5°$ from the zenith can introduce measurement errors of broadband downwelling irradiance larger than 100 W·m^{-2} (Long et al., 2010) or up to 15% of total irradiance, which will propagate in the surface reflectance-factor estimates.

To estimate the incoming downwelling radiation field under constant irradiance conditions, a white Lambertian reflectance panel at the ground and measuring the radiation at the beginning or end of the flight is a widely used and simple method (Aasen and Bolten, 2018). However, under passing clouds, the downwelling irradiance can change by a factor of ten, and a continuously measuring ground based sensor, a solution provided by Burkart et al. (2014), will miss spatial differences within distances of few meters. Some studies solve this by fixing an incoming light sensor (ILS) on top of the UAS (Hakala et al., 2018) but this introduces another error due tilting of the UAS. Correcting for such errors is specially challenging under intermittent clouds, when the diffuse radiation fraction changes dynamically and different fractions of the sky hemisphere are viewed by the ILS. Some studies have developed a sensor-based approach to this problem by measuring diffuse and direct fractions (Long et al., 2010) or interpolating the irradiance field over the hemisphere with multiple sensors (Suomalainen et al., 2018). Others, like Boers et al. (1998) estimated the angular distribution of downwelling irradiance using a radiative transfer model. However, the modeling approach still needs to be adapted for where the total diffuse and direct radiation field also changes, as the exact position of the clouds in the sky in relation to the sensor is unknown.

This paper aims to advance the use of UAS for hyperspectral imaging in all-weather conditions providing accurate reflectance-factor estimates at the surface. The main objective is to demonstrate a novel data-driven method to correct spectral irradiance for platform tilting under intermittent cloud cover conditions. The method relies on the Lambert cosine law and exploits the high-frequency irradiance variations caused by wind gusts. It simultaneously accounts for changes in diffuse and direct radiation due to cloudiness and to platform attitude changes due to wind gusts and flight direction. As part of the methodology to map the

surface reflectance-factors, a radiometric and spectral calibration workflow was applied to the hyperspectral radiance imager.

In this study, spectral radiance and downwelling irradiance datasets were collected over the Palo Verde National Park wetlands, a Ramsar site, in Costa Rica during November 2018. Two miniaturized HS sensors were used: a Cubert Firefly VIS-NIR hyperspectral sensor and an OceanOptics VIS-NIR spectrophotometer attached to the UAS. This study is part of a research project to assess vegetation functional diversity and drivers of encroaching vegetation in the Palo Verde wetlands.

We expect that the methodologies of UAV hyperspectral sensing developed in this study will contribute to answering scientific questions related to biodiversity losses, assessment of functional and structural traits of vegetation, or evaluate ecosystem degradation and responses to disturbances in terrestrial and aquatic systems with unprecedented spatial details.

2. Unmanned Aerial System

The flight platform used is a DJI Matrice 600 Pro hexacopter. It supports autonomous flight operations to follow a pre-programmed flight route. It has a maximum payload capacity of up to 5.5 kg and a maximum flight time of 38 min without payload, reduced to 18 min when utilizing the maximum payload capacity. Three Global Navigation Satellite System (GNSS) receivers are installed with one antenna each, which are used to determine and log the platform's absolute position during flight. Furthermore, three Inertial Measurement Units (IMU) are installed, which are used in conjunction with the GNSS data to calculate the platform's attitude (three-axis orientation in space). Both the platform position and attitude are recorded with a frequency of 100 Hz.

Upwelling hyperspectral radiance was measured with the miniaturized snapshot imager Cubert Fireflye 185 (Cubert GmbH, Germany), which has a global shutter. It has 138 bands in the visible to near-infrared spectrum (VIS-NIR, 450 nm – 950 nm) and an image size of 50×50 pixels. The dynamic range of the hyperspectral data is 12 bits. Additionally, a greyscale image is acquired, which has a larger image size of 1000×1000 pixels, which can be used for pan-sharpening the hyperspectral data or to align and geo-reference the hyperspectral data. A lens with a focal length of 23 mm was used with the camera, which results in a field of view of $15°$. The maximum frequency of image acquisition achieved under survey conditions was 0.5 Hz. The low weight of 490 g is optimal to employ the camera onboard an UAS. The camera was mounted on a Gremsy T3 gimbal (Gremsy, Vietnam) below the UAS, to ensure it is always nadir looking.

To measure spectral downwelling irradiance, an Incoming Light Sensor (ILS) was installed upwards-looking without a gimbal, thus experiencing the same pitch, roll and yaw as the UAS. The ILS consisted of a FLAME-S-VIS-NIR spectroradiometer, using a CC-3-DA cosine corrector with Spectralon diffuser as fore-optic (Ocean Optics BV, Netherlands). The spectroradiometer was spectrally and radiometrically calibrated by the manufacturer (spectral accuracy: < 0.04 nm; radiometric accuracy: $< 1\%$). It has 2048 spectral bands in the 350–1000 nm range with a spectral resolution of 1.33 nm full width half maximum (FWHM). The typical data acquisition rate under survey conditions is 5 Hz.

3. Data acquisition

The downwelling irradiance data and hyperspectral data presented in this paper were collected over a wetland at a section of the Palo Verde National Park in Guanacaste, at the Northern Pacific coast of Costa Rica which is part of the Ramsar Wetland convention (see Fig. 1b). The covered section had contrasting surfaces with open water and different wetland plant functional types, namely vegetation patches dominated by southern cattail (*Typha domingensis*), fire flag (*Thalia geniculata*), spike rush (*Eleocharis* ssp.), water hyacinth (*Eichhornia crassipes*), palo verde trees (*Parkinsonia aculeata*), as well as generalized riparian forest
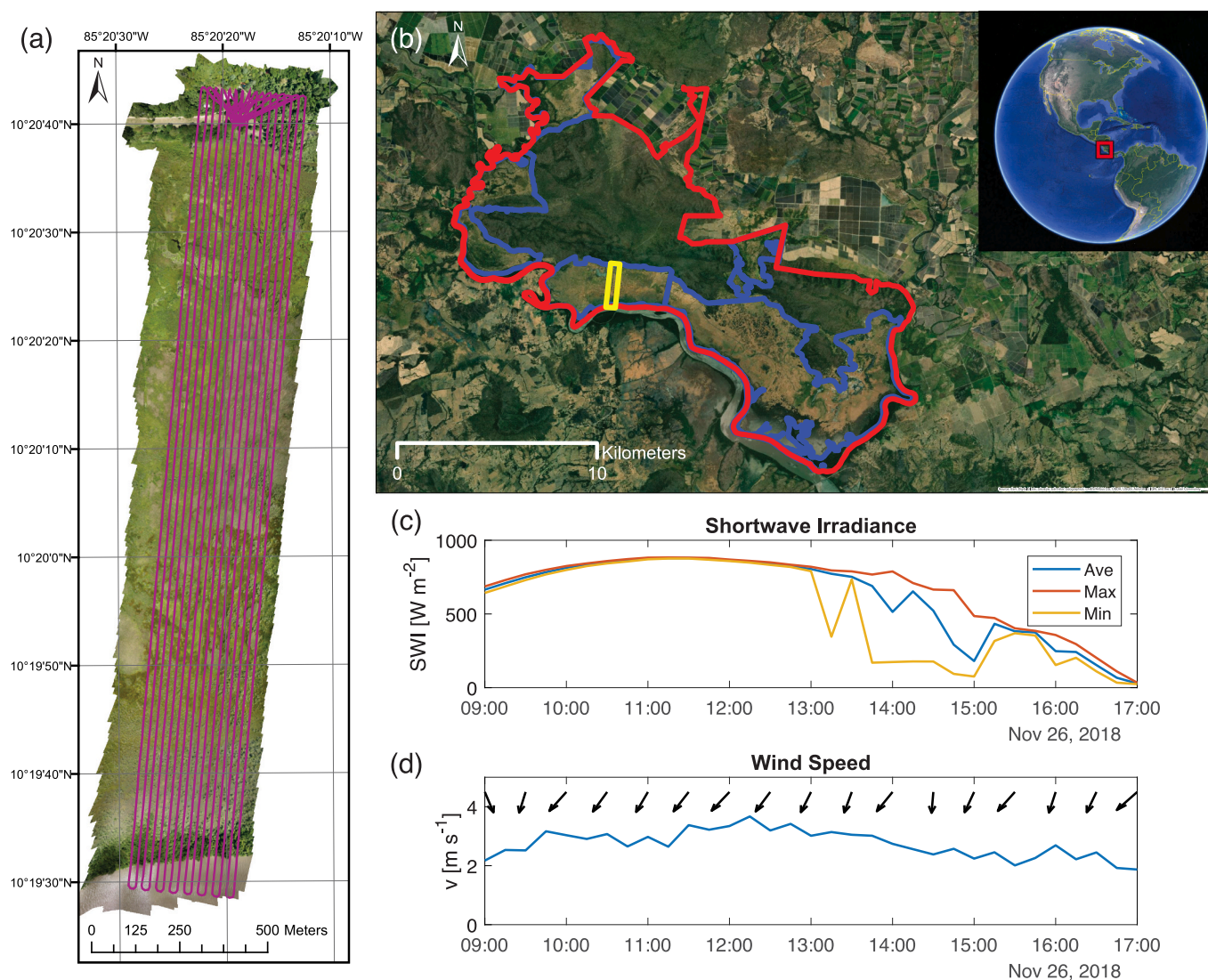
Fig. 1. (a) Purple line shows the flight routes of the UAS for data collection over the investigated area of Palo Verde Wetland. (b) The Palo Verde National Park is outlined in red, while the wetland area is outlined in blue. The investigated flight area is marked with a yellow rectangle. (c) Meteorological conditions were measured by a permanent meteorological station within the survey area during UAS data acquisition. Shortwave irradiance variation was low in the morning during clear sky conditions. Variation increased with intermittent cloud cover. (d) Wind speed and wind direction (black arrows) were stable during the flight campaign. (For interpretation of the references to colour in this figure legend, the reader is referred to the web version of this article.)

and wet meadow.

The data was collected on November 26th, 2018 between 9 a.m. and 5 p.m. during 8 separate flights. The total area covered was approximately 450×2200 m (ca. 100 ha). Flights were conducted in a scanning stripe pattern with flight directions alternating between north to south and south to north and a distance of 25 m between the flight lines (Fig. 1a). The average flight altitude was 150 m with an average flight speed of 10 m·s^{-1}, resulting in a ground sampling distance (GSD) of 79 cm·pix^{-1}, a front overlap between images of 50% and a side overlap of 38%. In total 15 measurements of downwelling irradiance were taken on the ground, by measuring the radiance of a horizontally placed white Spectralon target (Labsphere, USA), which has a nominal Lambertian reflectance of 100%, with an ASD Handheld 2 spectrophotometer (Malvern Panalytical, USA). To convert ASD measured white panel radiance to downwelling irradiance, it was multiplied by a factor of π. Downwelling irradiance was measured shortly after take-off or shortly before landing of the UAS, when it was close to the location of ground-based irradiance measurement. Shortwave irradiance data from a permanent meteorological station within the survey area showed that sky

conditions were changing from clear sky in the morning to intermittent cloud cover after 1:15 p.m. (Fig. 1c). The average wind speed varied between 1.9 m·s^{-1} and 3.7 m·s^{-1}, with the wind coming predominantly from a northern to northeastern direction (Fig. 1d).

4. Methods

To calculate the reflectance-factor of the land surface, the upwelling radiance *L*, measured by the hyperspectral camera on board the UAS, was divided by the corrected downwelling irradiance *E* (Schaepman-Strub et al., 2006):

$$R(\lambda) = \frac{\pi L(\lambda)}{E(\lambda)} \tag{1}$$

To retrieve accurate at-sensor reflectance-factor maps, both *E* and *L* need to be as accurate as possible. The next section, therefore, explains the laboratory calibration of the hyperspectral camera, as well as the calibration and data correction regarding the ILS measuring the down-welling irradiance. A workflow was developed to account for changes in

downwelling irradiance unrelated to atmospheric variations, solely due to sensor attitude changes, and changes related to atmospheric variations due to passing intermittent clouds.

4.1. Spectral calibration of hyperspectral camera

The purpose of the spectral calibration was to precisely determine the spectral band response for each of the 138 bands of the hyperspectral camera, including the band center and the band width, defined by the FWHM of the response function, as this information was only provided for three bands by the manufacturer.

First, the spectral response of the hyperspectral camera was characterized by scanning a narrowband light source through the spectral range of the hyperspectral camera. The experimental setup (see Fig. 2a) consisted of a broadband 100 W Quartz Tungsten Halogen light source (IL1, Bentham, UK) connected to a monochromator (TMc300, Bentham, UK) with a 0.2 nm wavelength accuracy. The output of the monochromator was connected through a fiber optical cable to a 15 cm diameter integrating sphere (UPB-150-ART, Gigahertz-Optik, Germany). The lens of the hyperspectral camera was attached to an optical port on the integrating sphere with an offset angle of 90° towards the incoming light. A spectroradiometer (ASD Handheld 2, Malvern Panalytical, USA) was connected to the integrating sphere as well, in order to measure the radiance in the sphere.

The wavelength of the monochromator changed from 440 nm to 1030 nm in 1 nm increments. For each wavelength setting, ten hyperspectral images were taken, as well as two radiance measurements with the spectroradiometer. The nominal integration time of the hyperspectral camera was set to the maximum exposure time of 1 s, as the maximum achievable light intensity in the integrating sphere is low, ranging from 0.005 W·m^{-2}·nm^{-1}·sr^{-1} to 0.03 W·m^{-2}·nm^{-1}·sr^{-1} for the different monochromator wavelength settings. The measurements were taken over the course of 3 days and at the end of each experimental day, dark current (DC) measurements were taken with the hyperspectral camera by turning off the light source.

To analyze the spectral response, the DC was subtracted from the measured hyperspectral digital number (DN), and thereafter the measurements were normalized by the irradiance of the light source measured with the ASD. All the instruments (Cubert camera, ASD, monochromator) were warmed up at least 30 min before the calibration. Even so, inconsistent dark current was observed during each day and from day to day. This inconsistence was further carefully corrected by applying a correction factor using the ratio of DN coming from dark bands (e.g. far from the light source wavelength) and the explicit end of day DC measurements, as a proxy to estimate changes in DC throughout the day.

The bands of the hyperspectral camera, which are more than 30 bands apart from the hyperspectral camera band with the highest measured intensity, were considered "dark bands" (b_{DC}). The hyperspectral band with the highest DN response was considered to be the band corresponding to λ_{mono} the wavelength of the monochromator. The b_{DC} bands were utilized to detect the increase in the DC signal. The ratio of the DN from the dark bands versus the dark current measurement provides the applied DC factor. The dark current correction was then applied using the equation:

$$DN_{DC}(x,y,b,\lambda_{mono}) = DN(x,y,b,\lambda_{mono}) - \frac{\sum\limits_{b=b_{DC}}\sum\limits_{x}\sum\limits_{y}DN(x,y,b,\lambda_{mono})}{\sum\limits_{b=b_{DC}}\sum\limits_{x}\sum\limits_{y}DC(x,y,b)}DC(x,y,b)$$

(2)

Where DN is the measured digital number of the hyperspectral imagery, DC the dark current measurement at the end of the day, DN_{DC} the hyperspectral response corrected for dark current, b the spectral dimension of the hyperspectral camera in discrete bands, and x and y its spatial measurement dimension.

To characterize the response function of each hyperspectral band, a normalization of the corrected hyperspectral DN_{DC} was done. DN_{DC} was averaged over its two spatial dimensions in order to increase the signal-to-noise ratio. Thereafter, the hyperspectral measurements were normalized by the measured radiance by the spectroradiometer (ASD) within the integrating sphere:

$$DN'(b,\lambda_{mono}) = \frac{\overline{DN_{DC}}(b,\lambda_{mono})}{L_{ASD}(\lambda_{mono})}$$

(3)

Where DN' is the normalized response of the hyperspectral camera, $\overline{DN_{DC}}(b,\lambda_{mono})$ the spatially averaged DN_{DC} and $L_{ASD}(\lambda_{mono})$ the radiance in the integrating sphere at λ_{mono}, measured with the ASD Handheld 2. To characterize each band's spectral response, it was fitted to a Gaussian normal distribution (Hakala et al., 2018):
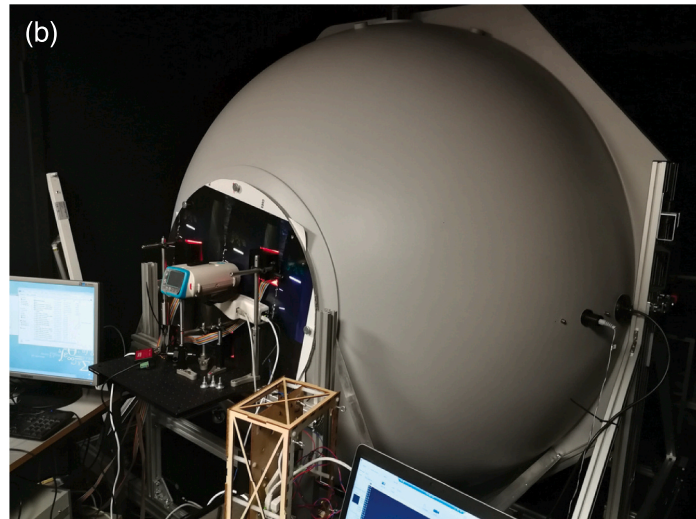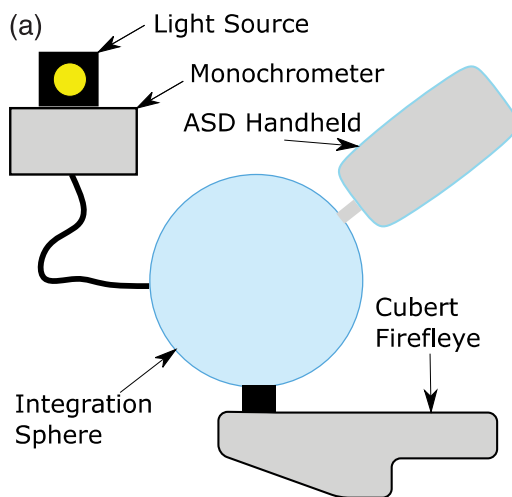

Fig. 2. (a) Schematic of the experimental setup to determine the spectral response of the hyperspectral camera. After passing the monochromator, the light from the light source reaches the integrating sphere through an optical fiber cable. The lenses of the hyperspectral camera and the spectroradiometer are attached to the integrating sphere's ports. (b) Setup for radiometric calibration of the hyperspectral camera. The hyperspectral camera, spectroradiometer and integrating sphere can be seen.

$$DN'(b, \lambda_{mono}) = h \exp\left(-4\ln(2)\left(\frac{\lambda_{mono} - \lambda_b}{FWHM_b}\right)^2\right) \quad (4)$$

With mean λ_b, FWHM and a generic fitting parameter h. The center wavelength of each band corresponds to λ_b.

4.2. Radiometric calibration of hyperspectral camera

In order to obtain physical spectral radiance L (W·m^{-2}·nm^{-1}·sr^{-1}), a radiometric calibration was performed to convert measured DN values into radiance. The setup of this calibration consisted of an integrating sphere with a diameter of 2 m (ISP2000, Instrument Systems, Germany), illuminated by 3 tungsten halogen lamps placed at the bottom inside the sphere and 6 broad-band emission LED-light sources with different emission peaks between 450 nm and 650 nm attached to the sphere's port. The hyperspectral camera was placed at the port of the sphere, as well as the ASD Handheld 2 spectroradiometer, in order to measure the illumination levels inside the sphere (see Fig. 2b). In order to reduce radiance loss and ensure even illumination, the 60 cm diameter sphere port was covered with a white sheet, which had fitted openings for the instruments (Wang et al., 2019a). The large diameter of the integrating sphere ensured a homogeneous illumination throughout the whole target area inside the 15° field of view of the hyperspectral camera. 9 different illumination settings were used for the calibration and the resulting spectral radiance in the integrating sphere, measured with the ASD, was between 0.02 W·m^{-2}·nm^{-1}·sr^{-1} and 0.22 W·m^{-2}·nm^{-1}·sr^{-1}. The illumination levels cover the range of expected target radiance levels in the environment, especially for low light conditions as found in Denmark, or low reflectance targets such as water surfaces.

For each illumination setting, the illumination was continuously monitored with the spectrophotometer while a series of hyperspectral cubes was acquired. The nominal integration time of the hyperspectral camera was varied from 0.1 ms to 100 ms, in variable intervals of 0.1 ms to 0.5 ms. Before and after each series of hyperspectral measurements, a series of DC measurements was taken with the same integration time settings. In total 1728 hyperspectral calibration cubes and 3456 dark current measurements were taken.

The spectral radiance measured with the spectrophotometer was integrated over the response for each hyperspectral camera band, found in the spectral calibration (Section 4.4.1), to match the band characteristics of the hyperspectral camera. The radiometric calibration was conducted for each spectral band and each spatial pixel. A pixel-wise calibration allows removing spatial effects as vignetting and to compensate for a non-uniform photo-sensor response. Therefore, the resulting calibration coefficients are three dimensional matrices of the same shape as the hyperspectral cubes. The following equation is used to fit the calibration parameters in order to convert DN measurements into spectral radiance (Wang et al., 2019a):

$$L = a \cdot t^{-b} \cdot (DN - DC) \quad (5)$$

Where L is the spectral radiance, a and b are empirical calibration factors, t the sensor's nominal integration time, DN the sensor's response value and DC the dark current of the sensor.

4.3. Directional response of incoming light sensor

In a situation where the only contribution to irradiance on the ILS sensor plane is radiance coming from one direction, the relationship between irradiance, radiance and incoming light direction can be described as (Pharr et al., 2017):

$$E = \cos(\theta) \cdot L \cdot \pi \quad (6)$$

Where E is the irradiance, L the radiance and θ the angle between the incoming radiance and the sensor's normal. As the diffuser of the ILS does not have perfect Lambertian properties, the measured irradiance I

deviates from the true irradiance E. Therefore, an additional correction factor f_a, which is a function of the angle and wavelength λ of the radiance, was introduced which describes the angular sensitivity of the sensor:

$$I(\theta, \lambda) = f_a(\theta, \lambda) \cdot \cos(\theta) \cdot L \cdot \pi \quad (7)$$

The angular sensitivity of the sensor was determined in the laboratory, by characterizing the change of measurement response to a constant light source while changing the incoming light angle of the light source. The light source used was a supercontinuum white light laser with collimated output (SuperK EXTREME EXR-20, NKT Photonics, Denmark). Two sets of off-axis parabolic mirrors were used to increase the light beam diameter, with each set expanding the diameter by a factor of three. This way, the final beam diameter was between 27 and 35 mm, depending on the wavelength, thus allowing for uniform illumination of the ILS. The ILS was mounted on a rotating stage to control the angle between the light source and diffuser surface.

The incoming light angle was varied from −90° to 90° in 2° increments for three measurement repetitions. For each incoming light angle in each repetition, 20 measurements with the ILS were taken. The integrating time used for the measurements was 35 ms, which corresponds to typical outdoor flight conditions. Each measurement consisted of 20 single measurements, averaged internally by the instrument.

4.4. Correction of attitude effects on incoming light sensor

Downwelling irradiance (E) can be determined by measuring the spectral irradiance on a cosine diffuser, oriented parallel to the horizontal earth's surface. Having the ILS mounted rigidly on top of the UAS leads to deviations in the orientation between the sensor's surface and the earth surface with changes of the UAS's attitude. Those sensor orientation changes introduce measurement errors. The UAS attitude variations have two main components: A high-frequency component, caused by the UAS flight control system trying to compensate for wind gusts and to keep the UAS on its programmed flight route. Those high-frequency variations are normally of small magnitude (resulting in irradiance measurement variations of ca. 5%). The other component is a systematic change of attitude based on the flight direction. To propel itself forward, a multirotor UAS has to tilt forward towards the flight direction and the yaw angle of the platform is changing with flight direction (Suomalainen et al., 2018). Every change in flight speed or flight direction changes the platform attitude systematically with a large magnitude compared to the high-frequency changes.

The downwelling irradiance has two main components: direct radiation (E_s), which is the solar radiation reaching the earth's surface on a direct path; and diffuse radiation (E_d), which reaches the earth's surface omnidirectional after Rayleigh scattering, or scattering by aerosols, for example in clouds (Long et al., 2010). For simplification, it was further assumed, that the diffuse radiation is uniform over the hemisphere, so that it is invariant to angular effects (Boers et al., 1998).

From there follows that the downwelling irradiance can be written as:

$$E = E_s + E_d \quad (8)$$

Where E is the total irradiance defined on a horizontal plane, E_s is the direct irradiance and E_d is the diffuse irradiance. Similarly, the sensor-measured irradiance I is the sum of a direct irradiance contribution I_s and indirect irradiance contribution I_d to the sensor reading. The sensor measurement is influenced by its angular sensitivity, the orientation of the senor in space and the position of the sun:

$$I\left(\overline{\Omega}, \overline{n}\right) = I_s\left(\overline{\Omega}, \overline{n}\right) + I_d \quad (9)$$

Where $\overline{\Omega}$ is the vector describing the direction of the sun and $\overline{n}$ is the vector normal to the sensor surface (see Fig. 3).

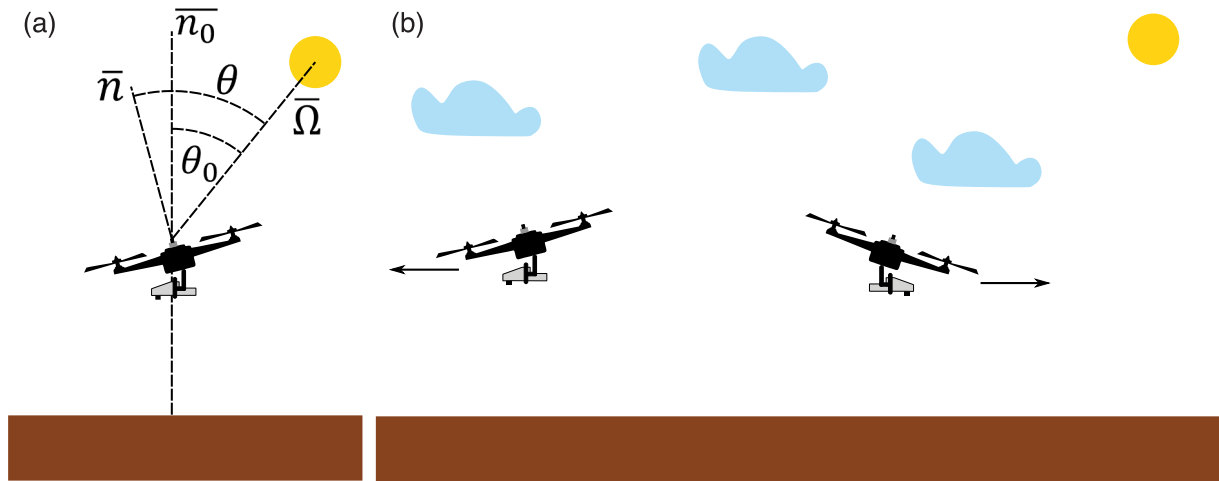To correct the measured I to retrieve the normalized-nadir irradiance

Fig. 3. (a) Schematic of angle and vector conventions. $\overline{\Omega}$ is the direction of the sun, $\overline{n_o}$ the zenith and $\overline{n}$ the direction normal to the ILS, while θ_0 is the zenith angle of the sun and θ the angle between the sun direction and ILS normal. (b) Different flight conditions during UAS survey. UAS is always tilting towards flight direction and therefore turning the ILS away or towards the sun. The direct/diffuse fraction of incoming light changes dynamically, depending on if there is a cloud in the direct pathway between UAS and the sun.

E, e.g. the one that would be measured if $\overline{n}$ was normal to the earth's surface (equal to $\overline{n_0}$), a correction factor f_s for the direct irradiance fraction and a correction factor f_d for the diffuse irradiance fraction was introduced to account for the tilting and angular sensitivity of the ILS sensor:

$$E = f_s(\theta,\theta_0){*}I_s\left(\overline{\Omega},\overline{n}\right) + f_d{*}I_d \tag{10}$$

Where θ_0 denotes the zenith angle of the sun and θ the angle between the sun direction $\overline{\Omega}$ and the sensor's normal $\overline{n}$. The factor f_d accounts for the change in ILS measurements due to the sensor's angular sensitivity, when the irradiance is diffuse (isotropic illumination), compared to when all irradiance is perpendicular to the sensor's surface:

$$f_d = \frac{\pi}{\int_0^{\pi/2}\int_{-\pi}^{\pi} f_a(\theta){*}cos(\theta)d\varphi d\theta} \tag{11}$$

The correction factor f_s takes into account the illumination change of the sensor based on the Lambertian cosine law (Pharr et al., 2017) and the effect of the angular response f_a of the sensor (see Eq. (7)). It was calculated as:

$$f_s(\theta,\theta_0) = \frac{cos\theta_0}{cos\theta}\frac{1}{f_a(\theta)} \tag{12}$$

The direction of the sun $\overline{\Omega}$ was calculated according to Reda and Andreas (2004), based on the sensor's geographical location, date and time. The sensor's normal was calculated based on the attitude observations of the IMU unit of the UAS (Glennie, 2008):

$$\overline{n} = \text{rotx}(\pi){*}\text{rotz}(\gamma){*}\text{roty}(\beta){*}\text{rotx}(\alpha){*}\begin{bmatrix} 0 \\ 0 \\ -1 \end{bmatrix} \tag{13}$$

rotx, roty and rotz denote the rotation matrixes around the x, y and z-axis respectively, while α, β, γ denote the roll, pitch and yaw angles of the UAS platform. The angle between the sun direction $\overline{\Omega}$ and the sensor's normal $\overline{n}$ can be expressed as:

$$cos\theta = \frac{\overline{\Omega}\cdot\overline{n}}{\left|\overline{\Omega}\right|\left|\overline{n}\right|} \tag{14}$$

4.4.1. Correction under constant irradiance conditions

The application of Eq. (11), to obtain E, requires estimates of how much of the measured I at a given moment in time is contributed by direct I_s and indirect I_d irradiance. As a first step we solve this problem for conditions of constant real world irradiance, for example under clear sky conditions, homogeneous cloud cover, or for short periods of time under intermittent cloud conditions, when the cloud configuration is nearly constant and the fraction of diffuse and direct irradiance is stable. It was hypothesized that, under those conditions, the main driver of measured downwelling irradiance I variations over time were the attitude variations of the UAS platform. Because of the assumption of constant real world irradiance, it follows that the variance σ^2 of the real-world irradiance can be assumed to be zero for these certain conditions. Based on this, it was further assumed that the correction of downwelling irradiance for this condition was optimal when the variance σ^2 of the corrected irradiance E over time was minimized. These assumptions were used to calculate I_s and I_d, and consequently E. To do so, based on Eq. (10), E was expressed as a function of I, I_d, f and g, by substituting I_s as the difference between I and I_d. This is applied for each spectral wavelength band of the ILS sensor:

$$E(t,I_d) = f_s(\theta_0(t),\theta(t)){*}(I(t) - I_d) + f_d{*}I_d \tag{15}$$

t denotes the time of the data collection. Because of the assumptions regarding constant irradiance conditions over time and the isotropic hemispherical distribution of the diffuse irradiance, the retrieved I_d is assumed to be constant over time. To find the spectral diffuse irradiance I_d, the variance of the corrected downwelling irradiance E was minimized with respect to I_d for each spectral band during the data acquisition time (t):

$$\min_{I_d} \sigma^2(E(t,I_d)) \tag{16}$$

After the sensor diffuse irradiance I_d is found, the sensor direct irradiance I_s can be extracted as well. This is based on the assumption that the constant real-world irradiance is equal to the mean μ of the corrected downwelling irradiance E with the previously found diffuse irradiance I_d as input. Therefore I_s is calculated as the difference of mean corrected irradiance E and diffuse sensor-based irradiance I_d:

$$I_s = \mu(E(t,I_d)) - I_d \tag{17}$$

Now Eq. (11) can be applied to correct the downwelling irradiance measurements for the sensor tilting effects.

4.4.2. Correction under temporally changing irradiance conditions

Under real-world data acquisition conditions, especially when flying under intermittent clouds, the downwelling irradiance and its diffuse and direct fractions are changing dynamically and constant irradiance cannot be assumed during the timespan of a typical UAS flight (for example 30 min). Here we propose a novel method to correct the downwelling irradiance measurements also under changing irradiance conditions for sensor tilting effects. In a first step, short time spans of a UAS flight (40–60 s) are identified during which the measured downwelling irradiance I is only exhibiting high-frequency variations and no long-term temporal trends. For those sections, the real irradiance E was assumed to be constant and any variations to be caused by small angular sensor movements. Therefore, for each identified section, the correction method for constant irradiance conditions could be applied. This was used to calculate diffuse I_d and direct sensor irradiance I_s spectra for each identified section.

In a second step, it was assumed, that the extracted I_d and I_s spectra represent characteristic irradiance spectra during different irradiance conditions during a UAS flight, and consequently can be regarded as spectral endmembers. It was hypothesized that each spectrum collected during an UAS flight can be represented as a linear combination of those endmembers:

$$\boldsymbol{i}(t) = \boldsymbol{V_s}\boldsymbol{s}(t) + \boldsymbol{V_d}\boldsymbol{d}(t) + \boldsymbol{\epsilon} \tag{18}$$

Where $\boldsymbol{i}(t)$ is the vector of the measured downwelling irradiance at time t, whose length corresponds to the number of spectral bands of the ILS sensor. $\boldsymbol{V_s}$ is a two dimensional matrix of size $k * j$ containing the endmember spectra of the direct radiation in columns, where k is the number of spectral bands and j is the number of different direct radiation endmembers, which corresponds to the number of flight sections with constant irradiance conditions identified. $\boldsymbol{V_d}$ contains the endmember spectra of diffuse radiation in the same manner and has the same dimensions. The vector $\boldsymbol{s}(t)$ of length j contains the relative contribution of the direct radiation endmembers to the total measured irradiance. $\boldsymbol{d}(t)$ of length j is the relative contribution of the diffuse radiation endmembers. The remaining residual is $\boldsymbol{\epsilon}$.

For each measured spectrum during the entire UAS flight, the relative contributions $\boldsymbol{s}(t)$ and $\boldsymbol{d}(t)$ of all the direct and diffuse endmembers were calculated by using a linear least-squares method to minimize the squared 2-norm of the residual $\boldsymbol{\epsilon}$ in Eq. (18). Explicitly:

$$\min_{\begin{bmatrix} \boldsymbol{s}(t) \\ \boldsymbol{d}(t) \end{bmatrix}} \left\| \begin{bmatrix} \boldsymbol{V_s} & \boldsymbol{V_d} \end{bmatrix} \begin{bmatrix} \boldsymbol{s}(t) \\ \boldsymbol{d}(t) \end{bmatrix} - \boldsymbol{i}(t) \right\|_2^2 \tag{19}$$

Having found $\boldsymbol{s}(t)$ and $\boldsymbol{d}(t)$ and therefore being able to calculate

direct and indirect irradiance contribution for each measured irradiance spectrum, allows applying Eq. (11), which finally yields the corrected irradiance $e(t)$ for each measured spectrum:

$$\boldsymbol{e}(t) = \boldsymbol{V_s}\boldsymbol{s}(t)*\boldsymbol{f_s}(\theta, \theta_0, t) + \boldsymbol{V_d}\boldsymbol{d}(t)*\boldsymbol{f_d} \tag{20}$$

An overview of the workflow is displayed in Fig. 4.

4.4.3. Identification of flight sections with constant irradiance

In the presented method, the number of sections with constant irradiance during one flight is variable and therefore the number of spectral endmembers of diffuse and direct irradiance is variable as well. In this study, it was chosen to identify two sections of constant irradiance per flight and therefore two endmembers of direct and indirect irradiance were extracted and used for each flight. Flight sections were chosen based on the following criteria: the length of each flight section should be between 40 s and 60 s and the variation in measured downwelling irradiance should only be of high frequency and random nature and not exhibit general temporal trends (e.g. variations in irradiance less than 9% worked well on this dataset as a threshold). Furthermore, to ensure that the spectral endmembers represented the different irradiance conditions during flight, one of the flight sections should have a high average measured downwelling irradiance (greater than 75% percentile of all measured values), while the other one should have low irradiance (smaller than 25% percentile of all measured values). In the case of a flight below intermittent clouds, this selection aimed to capture direct sun irradiance on the sensor versus the UAS flying below a cloud. If no intermittent clouds were present, this selection method ensured the analyzed flight sections represent different flight directions of the scan lines.

5. Results

5.1. Spectral calibration of hyperspectral camera

The spectral response of each band of the hyperspectral camera follows a Gaussian distribution very well. The coefficient of determination (R^2) of fitting each band's response to a Gaussian distribution (see Eq. (5)) lies between 0.989 and 0.999 (see Fig. 5b). The best fit is achieved for the central bands of the camera (band 20 to 131), which all have an R^2 value above 0.997. The shorter wavelengths have a moderate decrease in R^2, while the most outer bands at the longest wavelengths have the largest decrease in R^2.

The higher the central wavelength of a hyperspectral band is, the broader is its spectral response, as can be seen in an increase of FWHM with increasing central wavelength (Fig. 6). The bands of the
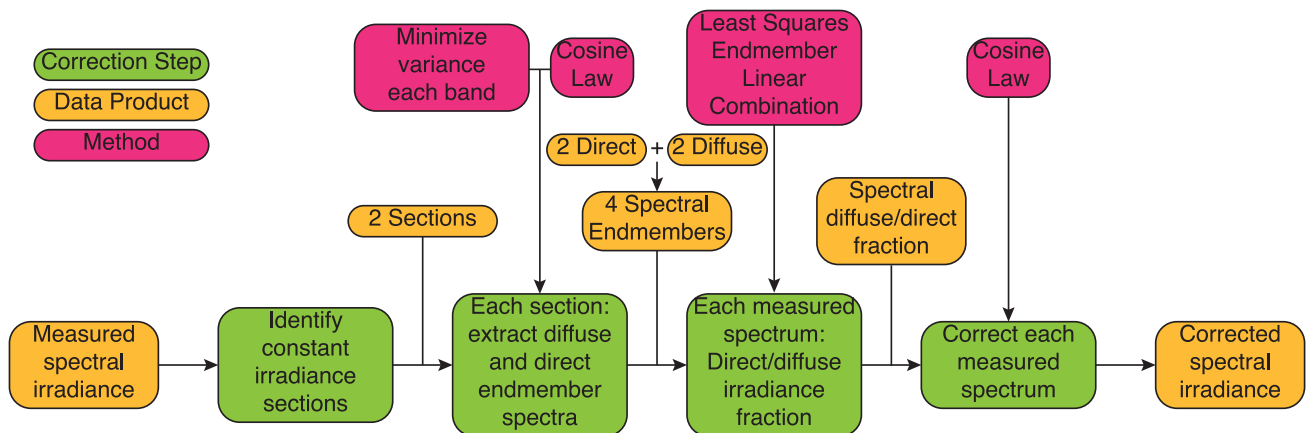

Fig. 4. Workflow to correct spectral downwelling irradiance for tilt effects under temporally changing irradiance conditions, for example under intermittent clouds. Workflow is divided into correction steps (green), data products (yellow) and underlying methods/principles (red). (For interpretation of the references to colour in this figure legend, the reader is referred to the web version of this article.)
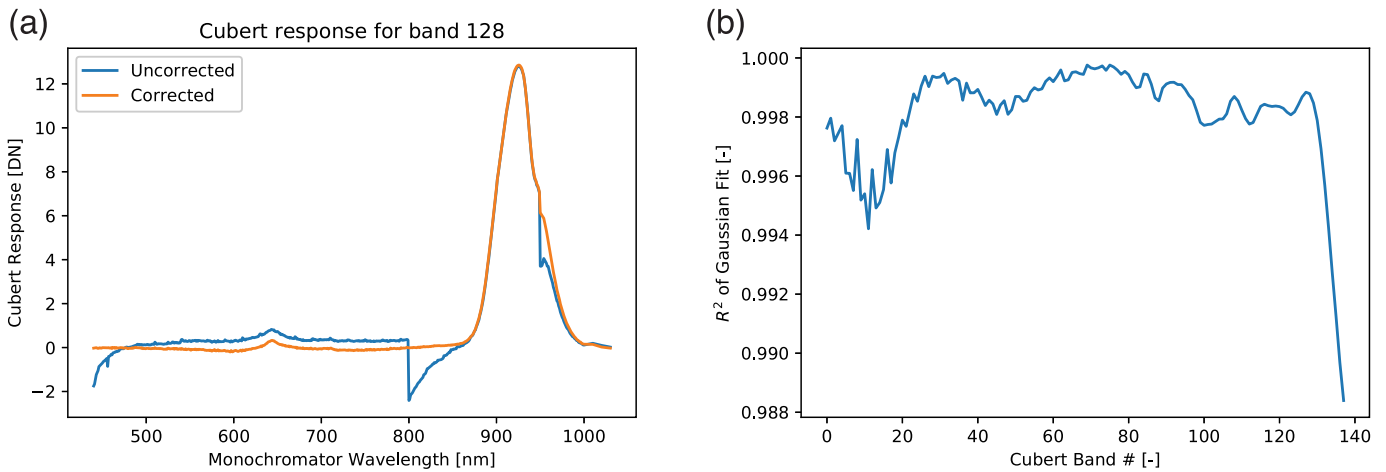
(a)

(b)

Fig. 5. (a) Response of hyperspectral camera band 128 to the monochromatic light source at different emission wavelengths. The blue line shows the response with constant dark current subtraction, while the orange line shows response after optimized dark current subtraction. (b) Coefficient of determination for the fit of each hyperspectral camera's band response to a normal Gaussian distribution. (For interpretation of the references to colour in this figure legend, the reader is referred to the web version of this article.)

(a)

(b)
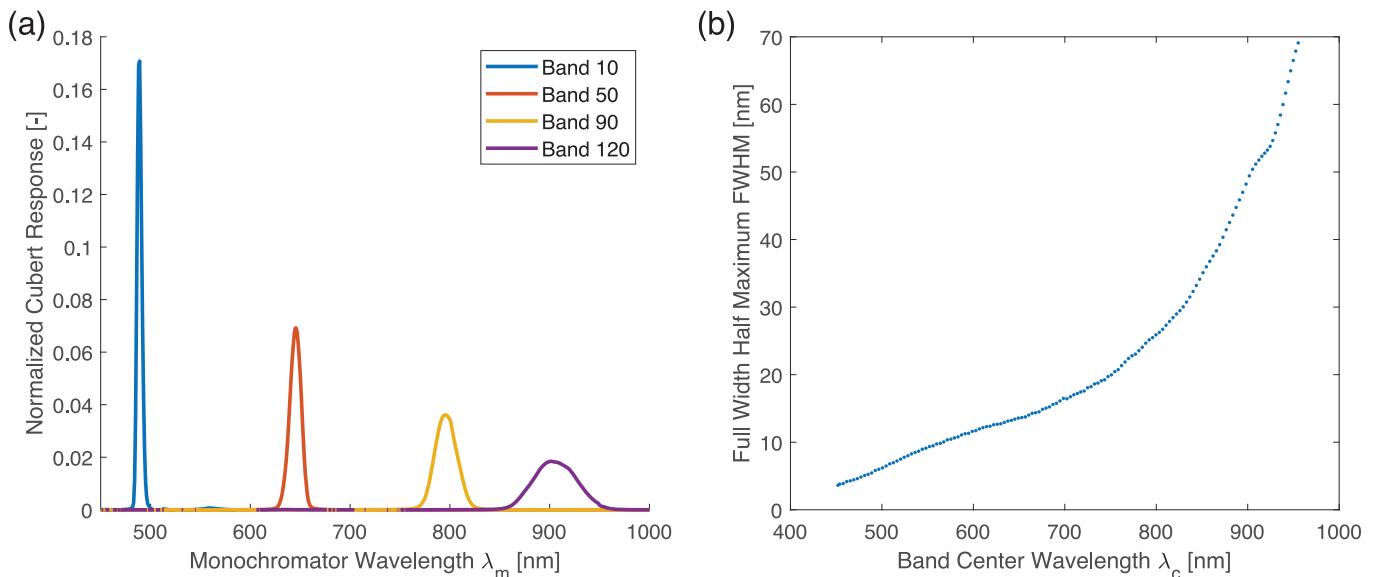
Fig. 6. (a) Spectral response of selected bands of the hyperspectral camera, normalized by their integral. Bands with a higher center wavelength have a broader response. The response of the individual bands follows a Gaussian distribution. (b) The resulting center wavelength and corresponding FWHM for each hyperspectral band.

hyperspectral camera range from a central wavelength of 451.87 nm to 955.20 nm, with an average step of 3.67 nm between the bands (range: 1.93–3.99 nm). The FWHM ranges from 3.63 nm to 69.10 nm, increasing with the bands' central wavelengths.

The monochromatic light source for the spectral calibration had a low intensity, which led to low response values of the hyperspectral camera, especially for the outer bands, which have a lower sensitivity than the camera's central bands. This can be seen for example in Fig. 5a, where the response of band number 128 is displayed. The maximum averaged response of this band is 12 DN, which is very low, compared to the 12 bits dynamic range of the camera (4096 DN). The effect of the dark current is relevant, especially as long integration times had to be used due to the low light source intensity. The calculated hyperspectral band response with constant subtracted DC exhibits three distinct features (at emission wavelength $\lambda = [440, 800; 950]$ nm), with an immediate drop of ca. 2 DN and a following slow increase. The drops occur at the beginning of each experimental day, with the hyperspectral camera

being cold and therefore having a low DC. With the instrument warming up, the DC is increasing. Applying the proposed correction method introduced in Eq. (2) removes those artifacts successfully, as can be seen comparing the corrected vs. uncorrected response in Fig. 5a.

5.2. Radiometric calibration of hyperspectral camera

Observing the response of the hyperspectral camera to a uniformly illuminated target shows large variations in response across the sensor's spatial dimension (see Fig. 7b). Some pixels deviate more than 50% from the mean of all pixels for a certain spectral band. Two dominating patterns in variations can be observed: the corners and sides of the image display a lower intensity, which is a typical vignetting effect. The most dominating effect is a vertical stripe/wave pattern. Similar effects for this camera model have also been reported by Aasen et al. (2014).

The Cubert camera DN values reached saturation with illumination intensity increasing. At low DN values, the relationship was close to
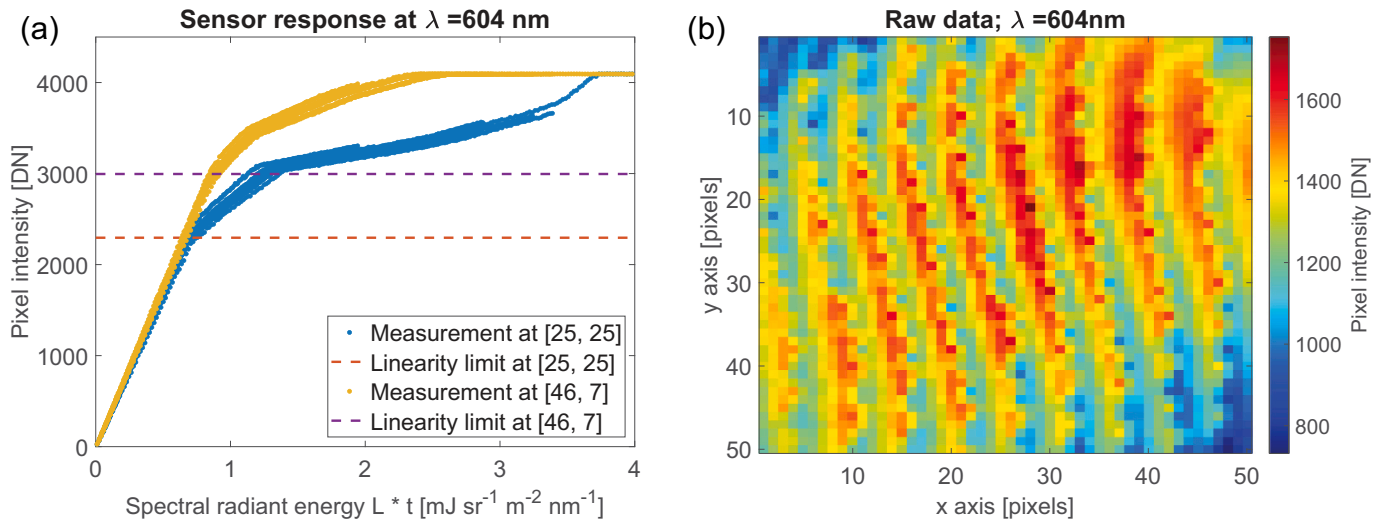
Fig. 7. (a) Investigation of linearity of hyperspectral camera response to increasing received radiative energy. Y-axis shows the response of the sensor, while the x-axis shows received radiative energy, which is computed by multiplying measured radiance with sensor nominal integration time. Data are plotted for two sample pixels of camera band 40, together with their respective limit of linearity. (b) Measured response of hyperspectral camera of band 40 of a uniform target with the spectral radiance of 0.138 W·m^{-2}·nm^{-1}·sr^{-1}, at the bands with central wavelength of 604 nm. The nominal integration time of sensor was 2.8 ms. Vignetting as well as vertical stripe/wave patterns in response are visible.

linear, but for increasing DN, a saturation effect was observed (see Fig. 7a). The onset point for saturation varies for each pixel and each band. The lowest observed linearity thresholds were at 1800 DN. Therefore, it was decided to operate the hyperspectral camera in a way, so that DN values above 1800 were avoided, reducing the sensor's real

dynamic range to 1800 DN (< 11 bit).

The spatial distribution of the calibration parameters can be seen in Fig. 8a+b, on the example of the camera's spectral band number 40 at a wavelength λ of 604 nm. Calibration parameter a shows spatial patterns, which are inverse to the observed response of a uniform target,
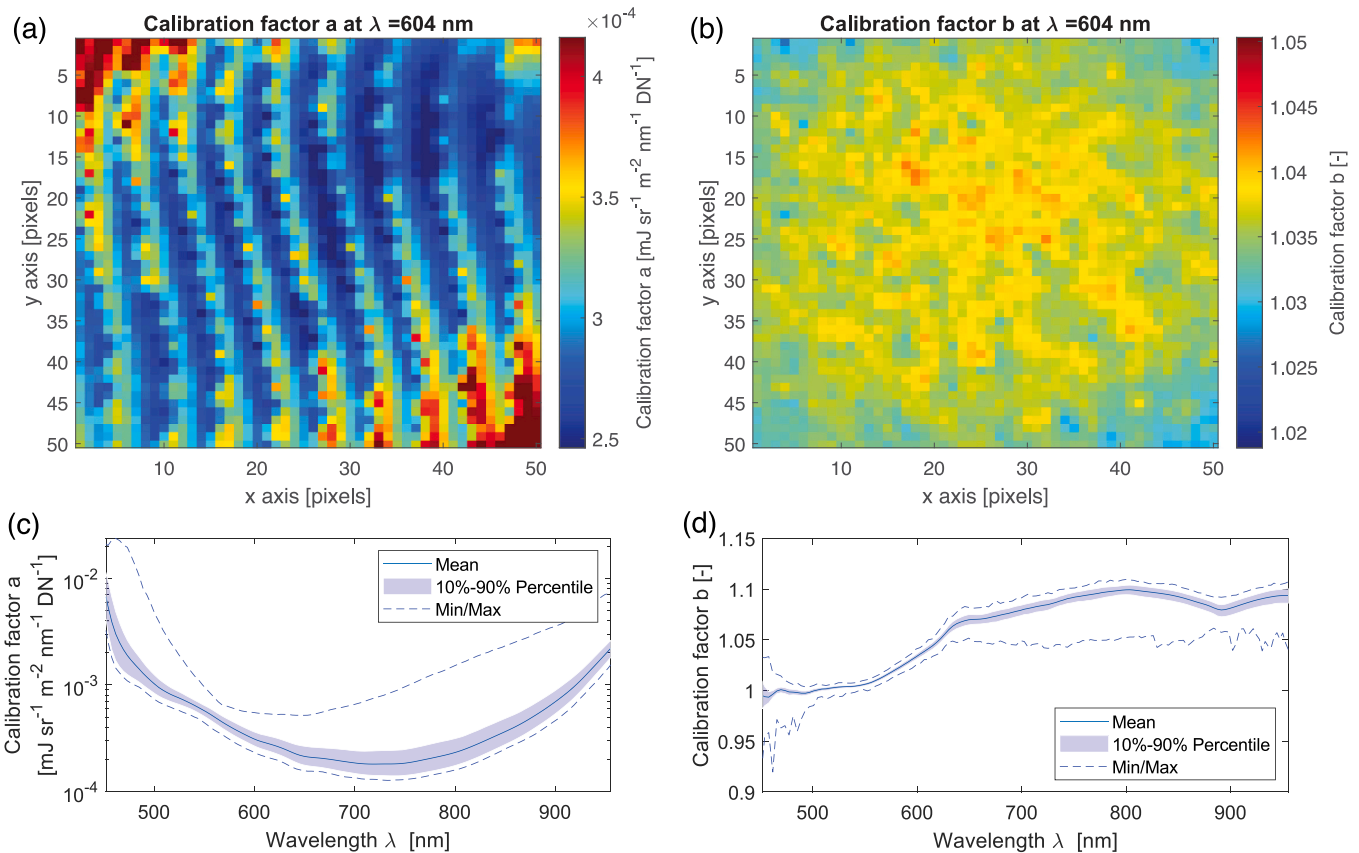

Fig. 8. Spatial variation of calibration factor a (a) and b (b) for band 40 (central wavelength 604 nm) of the hyperspectral camera. Variation of calibration factor a (c) and b (d) across the spectral range of the hyperspectral camera. The mean value of all pixels in each band, as well as 10%, 90% percentile and min/max values are displayed. Y-scale for factor a is logarithmic.

accounting for the different sensitivity of the different pixels. The spatial variation of calibration parameter *b* is small and does not exhibit clear patterns.

The sensitivity of the sensor, which has an inverse relationship with calibration factor *a*, varies by up to two orders of magnitude across the spectral range of the sensor. The bands with central wavelengths between 600 nm and 800 nm have the lowest values of factor *a*, and therefore the highest sensitivity. The variation across single pixels within each band is small within the 10% to 90% percentile, but few pixel outliers have values up to one magnitude higher than the band average. The calibration factor *b* shows only small variations across the spectral range of the hyperspectral camera. At the spectral band with the lowest wavelength, it has a value around 1, which is increasing to 1.1 for the spectral bands with a higher wavelength. The variation of this factor across pixels is also small for each band.

The goodness of fit of the collected calibration data compared to the calibration model can be seen in Fig. S1. Comparing the resulting relative RMSE (rRMSE) to DN measured by the hyperspectral camera shows that the calibration error is lowest between 500 DN and 1800 DN with an rRMSE of ca. 5%. For lower DNs, the rRMSE increases to up to 20%, which can be explained by a decreasing signal to noise ratio. For higher DNs, the rRMSE increases to above 50%, which is caused by the non-linear behavior of the camera for high DN values. The spectral bands from 475 nm to 820 nm have a low rRMSE, smaller than 6%, while the bands of higher and lower wavelengths have an increasing rRMSE, which is caused by a decreasing sensor sensitivity.

5.3. Directional response of incoming light sensor

The angular sensitivity f_a of the ILS is depending both on the wavelength and the angle between the incoming light and sensor diffusor surface (see Eq. (9)). For incoming light angle deviations from the sensor normal lower than 24°, the angular sensitivity is greater than 0.95 for all wavelengths, while f_a averaged over all wavelengths is greater than 0.9 for angles below 78° (see Fig. 9). From an angular deviation greater than 82°, the angular sensitivity falls off quickly and from an angular deviation greater than 86°, no light reaches the sensor. The wavelength range 620 nm to 935 nm has f_a values closer to 1, while for the outer wavelengths, the ILS response is deviating greater from the theoretical cosine response.

The measurement error between measurement repetitions can be considered small, with the resulting standard deviation for f_a between 0.001 and 0.11 (mean = 0.019). The sensor response depends on the rotation direction (positive angles vs. negative angles), which can be observed in the asymmetric behavior of f_a. That means for the given sensor, f_a is also a function of the azimuth. Also, when calculating f_a based on the absolute incoming light angle, omitting the rotation direction, the standard deviation lies between 0.002 and 0.217 (mean = 0.031), which is in its maximum around two times higher than the standard deviation based on the rotation directional angle.

For further analysis, the f_a factor based on the absolute incoming light angle is used, as the azimuth angle of the sensor in the UAS setup is unknown.

Calculating the influence of the angular sensitivity on diffuse irradiance ($1/f_d$, compare Eq. (11)) gives a value of 0.928, averaged over the investigated wavelengths.

5.4. Correction of attitude effects on incoming light sensor

5.4.1. Application of the irradiance correction method based on spectral unmixing

This *se*ction presents the correction of the downwelling irradiance data for both a flight during sunny conditions and a flight below intermittent clouds.

5.4.1.1. Sunny conditions. During a sunny flight, the uncorrected downwelling irradiance signal exhibited high-frequency variations and systematic shifts caused by the flight direction. In Fig. 10, the spectral downwelling irradiance is displayed as the total integrated broadband irradiance from 375 nm to 965 nm for ease of display. At the time of flight, between 8:34 AM and 8:41 AM local time, the sun was positioned in a south-eastern direction with an azimuth angle of 126° and an elevation of 37°. For the first 280 s of the flight, the UAS had a heading of 188° and an average pitch of −6.6°, heading south towards the sun and therefore pointing the ILS sensor towards the sun. During that flight section, the effects of tilting the sensor towards the sun and the ILS angular sensitivity counteracted on each other, which lead to an average value of 1.0 for f_s. For the last part of the flight, the UAS flew in the opposite direction, pointing the sensor away from the sun, which resulted in an average correction factor f_s of 1.27, increasing the measured irradiance for correction.

Before applying the correction, the broadband downwelling irradiance for the first section of the flight was 402 W·m^{-2}, while it was 313 W·m^{-2} for the second section. That means the measurements had an average difference of 89 W·m^{-2} (24.9%), caused by the direction of the flight and not an actual change in downwelling irradiance. After
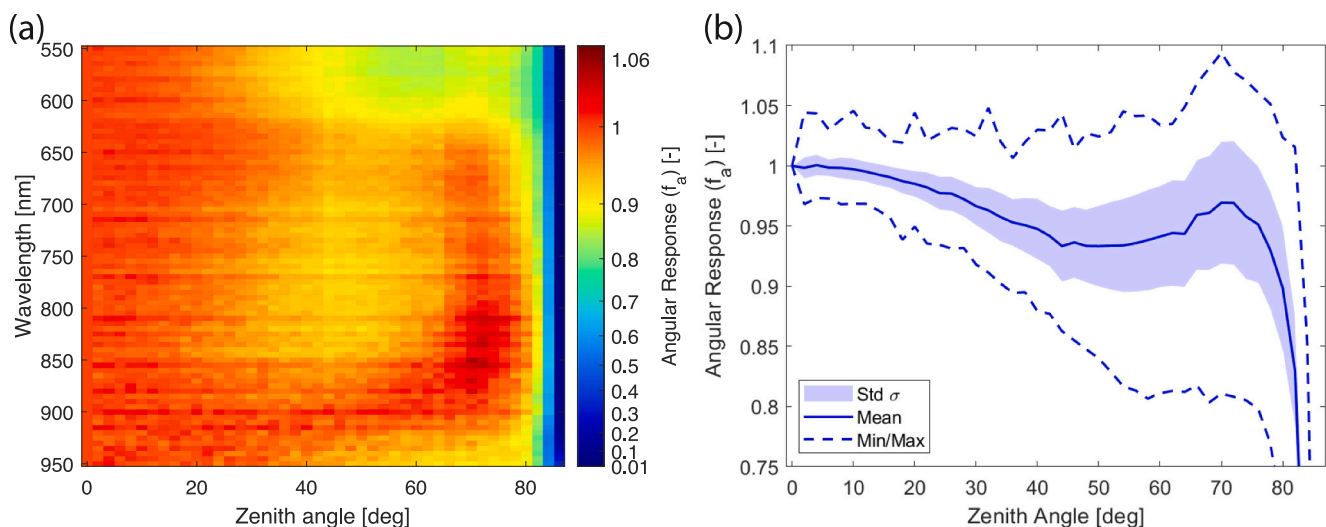

Fig. 9. Relative angular response of cosine receptor. Panel (a) shows the angular response f_a depending on incidence light wavelength and incidence angle. Panel (b) shows mean f_a and its standard deviation, minimum and maximum over wavelength, depending on incidence angle.
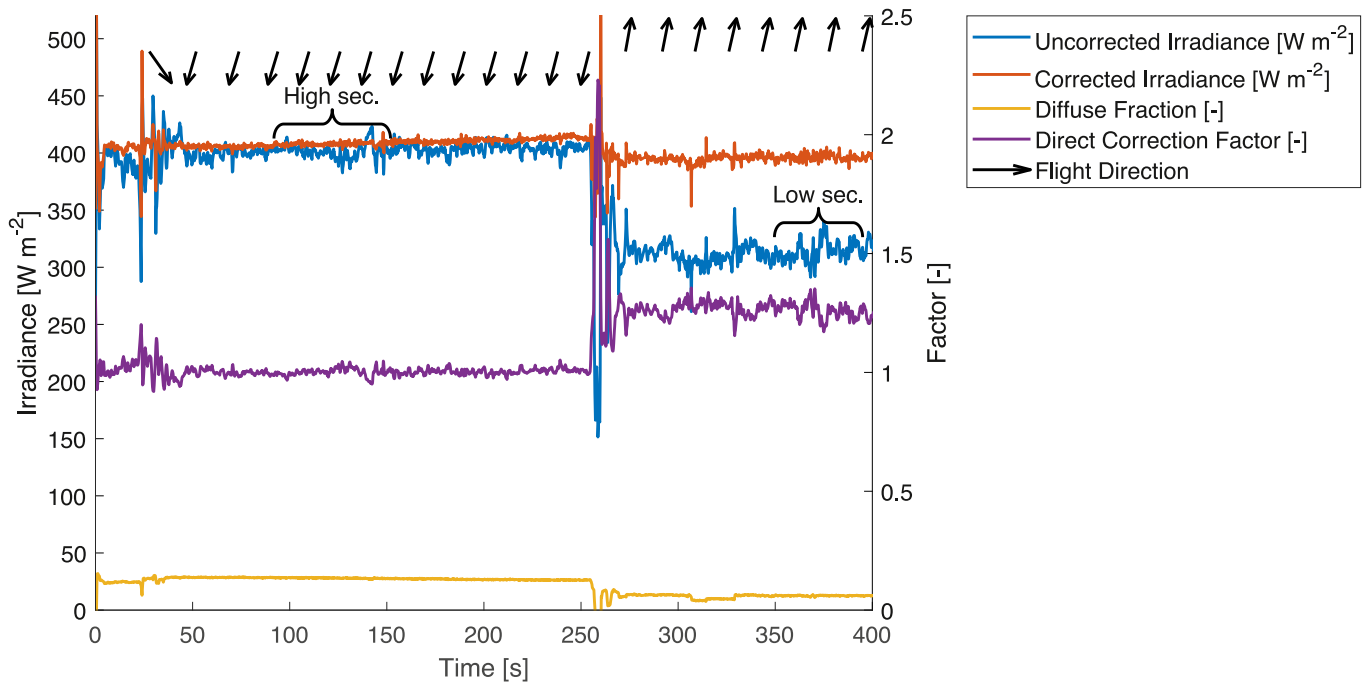
Fig. 10. Comparison of corrected and uncorrected broadband downwelling irradiance under sunny flight conditions. Uncorrected data shows an intensity jump at 260 s, caused by a flight direction change of the UAS. Applying the correction removes the jump and reduces high-frequency variations of the signal. The diffuse fraction is low throughout the flight. Flight sections for endmember extraction are marked as high sec. and low sec.

applying the correction, the first and last flight section had an average broadband downwelling irradiance of 408 W·m^{-2} and 396 W·m^{-2} respectively, meaning the difference between the two flight sections was reduced to 12 W·m^{-2} (3%), which corresponds to a reduction in difference compared to the uncorrected data of 87%.

The application of the correction method also reduced the high-frequency measurement variations of the downwelling irradiance data. The measured downwelling irradiance, after application of a high pass filter with a cut-off frequency of 0.1 Hz, had a standard deviation of

4.5 W·m^{-2} for the first flight section and 6.2 W·m^{-2} for the last flight section. This was reduced to 1.3 W·m^{-2} and 2.9 W·m^{-2} respectively after the application of our novel unmixing modeling approach, which corresponds to a reduction of 71% and 53%. The calculated fraction of diffuse radiation was below 0.16 throughout the entire investigated flight section, with a mean value of 0.1 and a standard deviation of 0.04.

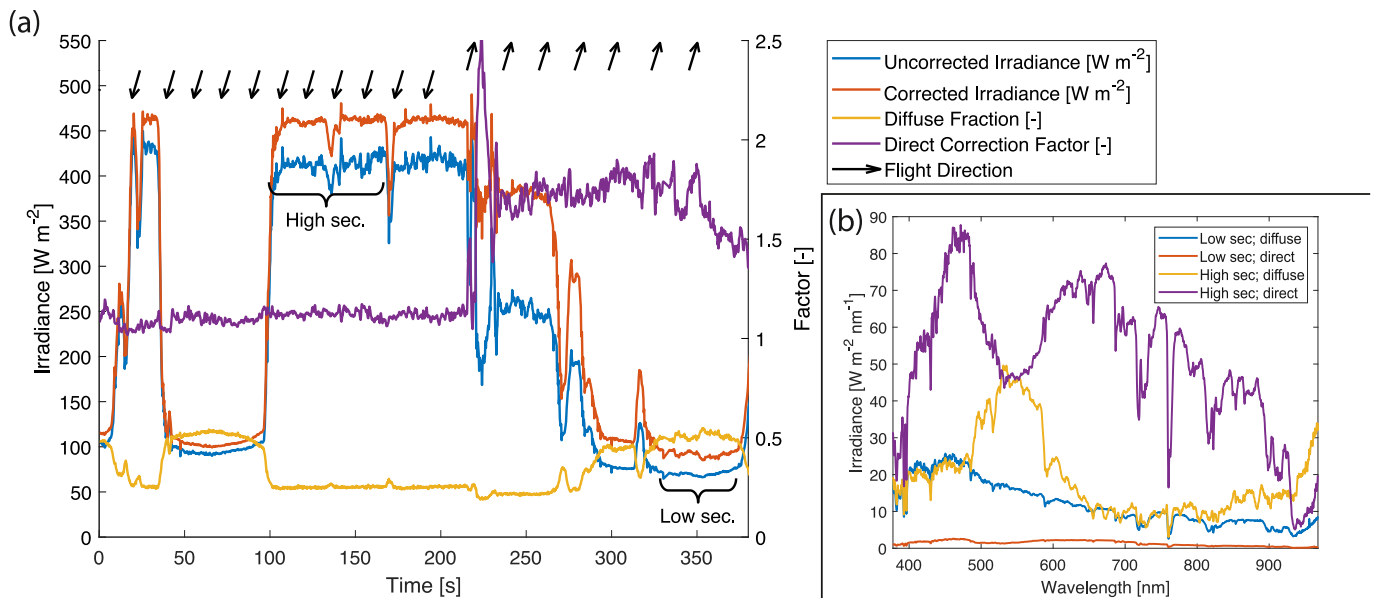*5.4.1.2. Intermittent clouds.* During a flight under intermittent clouds,

Fig. 11. (a) Correction of downwelling irradiance under intermittent clouds. Flight direction changed at 220 s, indicated by the change of correction factor. The uncorrected signal is dominated by changing clouds and change in flight direction. Applying the correction changes the intensity in the last half of the flight under sunny conditions drastically and reduces high frequency variations overall. Diffuse fraction changes with cloud cover between 0.19 (sunny) and 0.55 (cloudy). Flight sections for endmember extraction are marked as high sec. and low sec. (b) The four resulting radiation endmembers used for correction of the irradiance of this UAS flight.

the measured downwelling irradiance signal was dominated by the changing presence of clouds in the direct pathway between the sensor and the sun (see Fig. 11). The local time of flight was between 2:19 PM and 2:25 PM. The sun was in a southwestern direction with an azimuth angle of 233° and an elevation of 38°. For the first 200 s of the flight, the UAS was flying in a southern direction with an average heading of 188° and an average pitch of −5.8°. During the second half of the flight, the UAS headed the opposite direction with an increased average pitch angle of −13.4°, caused by wind from a northern direction, which leads to the ILS sensor facing away from the sun, which is indicated by the high correction factor f_s during this time (average: 1.71).

The computed diffuse radiation fraction varied between 0.19 and 0.55, with low values during sunny periods with high measured downwelling irradiance and high values during shaded periods with low measured downwelling irradiance. In the first flight section with an average correction factor f_s around 1.11, the corrected downwelling irradiance follows the measured irradiance closely with a slightly higher amplitude, while the high-frequency variations are reduced. In the second flight section, corrected and measured irradiance amplitudes were quite similar during cloudy periods, even though the correction factor f_s was well above 1. This is expected, as during cloudy periods the downwelling irradiance is mainly diffuse, which is invariant to the sensor's attitude. During the sunny periods, the corrected irradiance was up to 58% above the measured irradiance, as the sensor is facing substantially away from the sun and the main contribution to the irradiance is direct irradiance.

Overall, the high-frequency variations in downwelling irradiance were reduced throughout the entire flight, while they were mostly present during sunny conditions.

5.4.2. Accuracy of the downwelling irradiance measurements

A good agreement was found when comparing the corrected broadband downwelling irradiance measured from the UAS to the ground-measured broadband downwelling irradiance, with a RMSE of 14.5 W·m² and an nRMSE of 2.78% (see Fig. 12a). This was an improvement compared to the uncorrected UAS measurements, which had a RMSE of 82.77 W·m² and an nRMSE of 15.85%. For most points, the uncorrected UAS-based irradiance underestimated the ground-measured irradiance and it showed a much greater scatter, compared to the corrected data. Solar zenith angles varied between 31.5° and 54.7° during data acquisition. Ground based measurements were taken during sunny conditions.
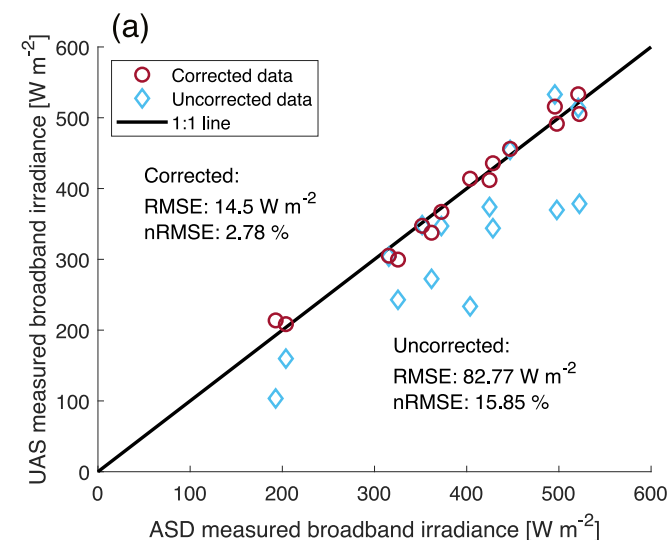
A sample spectrum of corrected irradiance measured by UAS, compared to the ground-measured irradiance showed a good agreement in the spectral shape for wavelengths greater than 600 nm (see Fig. 12b). For wavelengths below 480 nm, the UAS-measured irradiance was slightly lower than the ground-measured irradiance, and for wavelengths between 480 nm and 600 nm it was slightly higher. The uncorrected UAS irradiance has a very similar spectral shape to the corrected UAS irradiance, but it has a lower amplitude. The resulting nRMSE between corrected UAS and ground-measured irradiance for this sample was 3.68% and the nRMSE between uncorrected UAS and ground-measured irradiance was 11.88%.
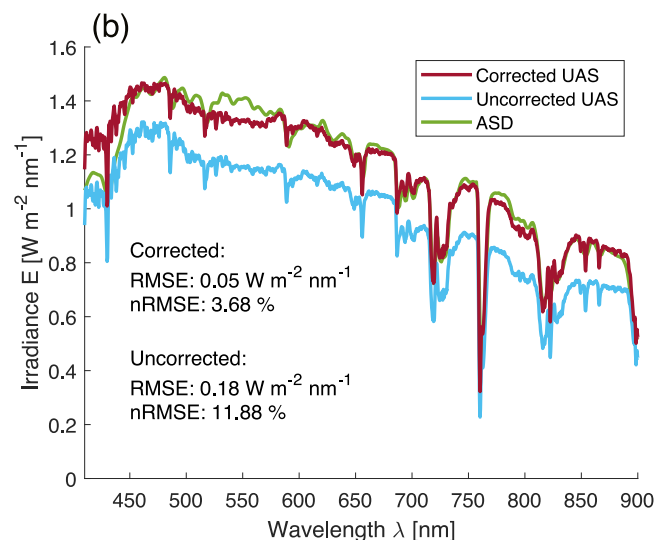
5.5. Effect of tilt correction on reflectance-factor mapping

Comparing resulting hyperspectral orthomosaic maps of reflectance-factor, calculated with raw downwelling irradiance data versus calculated with downwelling irradiance data corrected for UAS attitude effects, shows the strong influence of the correction on the final reflectance-factor product. Map (a) in Fig. 13, with data acquired during sunny conditions, shows a strong striping effect of land surface reflectance-factor, calculated with raw downwelling irradiance. At the time of flight, the sun had a southern azimuth angle and the UAS was flying consecutively in southern and northern directions. With the UAS flying in a southern direction and with the UAS tilting towards south and the sun, the downwelling irradiance is overestimated, and therefore the reflectance-factor is underestimated. When flying in a northern direction, the effects are inverted and the reflectance-factor is overestimated. Applying the attitude correction to the downwelling irradiance data counteracts those effects, and the striping effect is significantly reduced, as can be seen in Fig. 13(b).

6. Discussion

It has been pointed out that the information of spectral response functions of the spectral sensors, even though it is key, tends to be quite limited (Aasen et al., 2018). In this study, we demonstrated a workflow for a miniaturized hyperspectral sensor that allows optimizing its functionality by characterizing the sensor limitations in terms of spectral and radiometric resolution and dynamic range. This information is key for planning flight missions and for implementing realistic data processing algorithms or radiative transfer models.

Similar to Brachmann et al. (2016) we used a monochromator for

Fig. 12. (a) Scatter plot of corrected and uncorrected broadband downwelling irradiance measurements by UAS compared to ground-based broadband irradiance measurements with Spectralon white panel and ASD handheld 2. (b) Spectral comparison of corrected and uncorrected UAS measured irradiance to ground-measured irradiance for one sample data point.
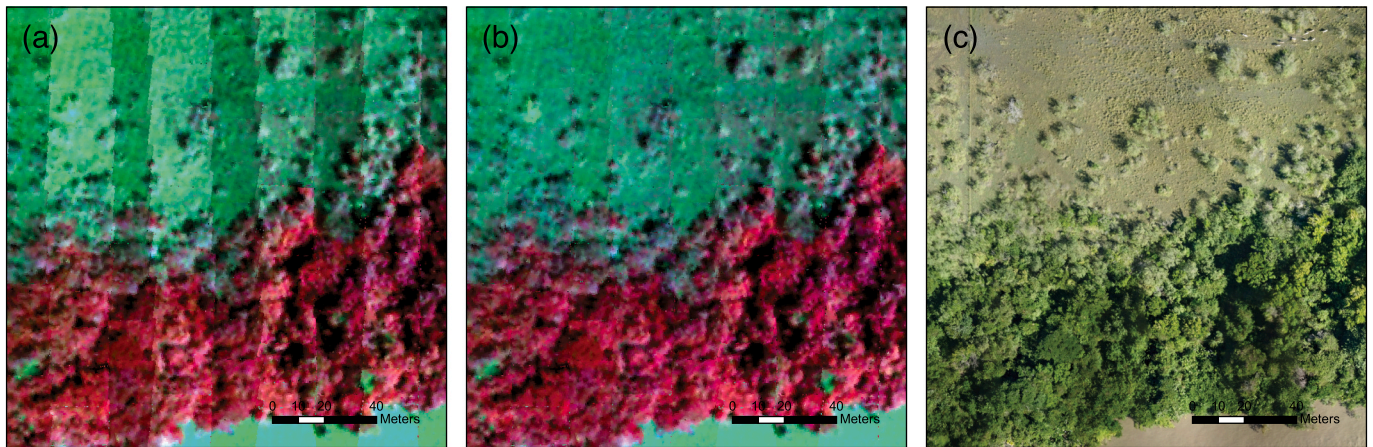
Fig. 13. False colour RGB representation of hyperspectral reflectance-factors (R: 844 nm; G: 493 nm; B: 560 nm), with data acquired during sunny conditions. In (a), no correction was applied to the downwelling irradiance for reflectance-factor calculations, whereas in (b), downwelling irradiance was corrected. The reflectance-factor in (a) is dominated by a striping effect, caused by the UAS flying alternating in north-south and south-north direction. Applying the correction to the downwelling irradiance data is reducing the striping strongly. (c) shows high resolution RGB map of the same area, acquired by UAS with a standard photo camera.

sensor calibration. Our spectral calibration of the CUBERT sensor showed a behavior with overlapping bands throughout the whole sensor spectral range. This effect was more pronounced in the NIR region due to an increasing FWHM that resulted in increased band overlapping with bandwidths more similar to that of a multispectral sensor. This will make it challenging to resolve fine spectral features in this region, as the number of separable spectral bands is strongly reduced. For example for a central wavelength of 452 nm, the FWHM is 3.63 nm, while at a central wavelength of 955 nm the FWHM is 69.1 nm with an average spectral sampling distance of 3.67 nm. The resulting spectral measurements have a higher actual spectral resolution in the visible range than in the near-infrared. The spectral response curves for each band of the hyperspectral camera fit the expected Gaussian distribution shape very well, with R^2 values above 0.989 for each spectral band, which is important as we use this function to approximate the spectral response in order to avoid implementing measurement noise into the spectral response function. Furthermore, this shows the validity of the developed corrections for low intensity of the light source in comparison to the sensitivity of the camera and the drifting over time of dark current in the experiment.

In our study, the absolute radiometric calibration of the hyperspectral CUBERT camera revealed large differences in the response of different pixels of the same spectral band to a uniform light source. Those differences are a combination of typical vignetting behavior, where, due to different path lengths of the light through the lens, pixels further from the center of the sensor receive less light and a pattern of vertical stripes. A similar striping pattern for this camera model has also been previously reported by Aasen et al. (2014). Those patterns are stable over time and therefore a pixel-wise calibration with unique calibration parameters for each pixel of each spectral band is advantageous, enabling to convert from measured digital number to physical radiance, regardless of the different pixel sensitivities. The calibration factor *b* having values close to one shows that the measured DN numbers increase nearly linear with the sensor's integration time for a constant illuminated target. The sensitivity is highest for the central bands, which also have the highest calibration accuracy, with a calibration error below 6% for spectral bands with wavelengths from 475 nm to 820 nm. During data acquisition in the field, the error in measured radiance might increase slightly compared to the calibration error, due to effects such as changing sensor temperature. Nonetheless, these results are close to the level of satellite hyperspectral mission requirements of <5% absolute radiometric error for the EnMAP, HyspIRI and PRISMA missions (Coppo et al., 2020; Guanter et al., 2009; Lee et al., 2015). Aasen et al. (2014) reported an absolute reflectance error for the same hyperspectral sensor of below 3%. Although this is not directly

comparable to our relative radiance error, the errors are similar in magnitude as can be expected. For example for a target with 50% reflectivity, an absolute error of 3% would correspond to a relative error of 6%. With a different type of sensor, Hakala et al. (2018) conducted a spectral calibration with their UAS-borne hyperspectral imager, and calibrated the sensor radiometrically bandwise, achieving an inflight relative reflectance root mean square error of below 7.6% in the visible range with higher errors in the infrared range. Both aforementioned studies reported their errors for field measurements, while the accuracy in this study is laboratory based. We also found that the actual dynamic range of the CUBERT camera is less than half of its theoretical or reported dynamic range. Therefore, during data acquisition in the field, the exposure time of the camera was controlled in a way such that DNs of 1800 were not exceeded, ensuring a predictable response of the camera.

We also proposed a novel data-driven model for correction of downwelling irradiance accounting for tilting and vibrations in the UAS platform due to turbulence effects under all-sky conditions. Even though flight instability from UAS is one of the main sources of error (Long et al., 2010), this topic has not received much attention yet, especially for both multispectral or hyperspectral reflectance-factor corrections. Our unmixing irradiance model relies on estimating endmembers of direct and diffuse radiation. We assumed that the intensity of diffuse radiation was constant over the whole sky hemisphere, similarly to (Long et al., 2010). In a real-world situation, the intensity of diffuse radiation has an angular dependency as well, even though to a much lesser extent than the direct radiation. Further sources of uncertainty in endmember calculation include the non-isotropic behavior of the ILS, and the effect that a small portion of land surface gets into the field of view of the ILS for high sensor tilt, which is not accounted for in the presented method or errors from the IMU measurements of the UAS platform. However, we addressed the potential effect of angular sensor responses. Characterizing the angular response of the hemispherical ILS showed that if the deviation of the incoming light from the sensor's normal is above 24°, the errors in sensor response are greater than 5% for some wavelength, compared to the theoretical cosine response and the errors increase rapidly with increasing angles. Under most flight conditions, especially UAS flights in the morning or afternoon in the tropics, or during most of the time in high latitude regions, the angle between the sensor's normal and the sun greatly exceeds 24°, leading to large errors in the sensor response. Therefore, the characterization of the ILS angular response is important for the angular corrections of the downwelling irradiance data, in order to correct for these shortcomings of the sensor. Furthermore, it showed that the sensor's angular response not only depends on the zenith angle of the incoming light, but also to a

lesser degree on the azimuth angle. As the characterization was only done as a function of the zenith angle, this is one source of uncertainty in correcting the downwelling irradiance data.

Applying the correction method for the downwelling irradiance on data collected during an UAS flight under clear sky conditions reduced a shift in measured irradiance, caused by a change in UAS flight direction, by 87%. The measured shift had an amplitude of ca. 24.9% of the measured average irradiance, which shows the high relevance of correcting this effect. After the model correction was applied, the shift represented only 3% (12 W·m^{-2}) of the downwelling irradiance and can be considered as an indicator of the in-flight stability in data correction. Furthermore, high-frequency variations in measured downwelling irradiance were reduced by more than 50%. This shows an effective filtering of effects caused by platform vibrations and turbulences. Comparing the corrected broadband irradiance to ground-based irradiance measurements yielded an nRMSE of 2.78%, which was a great improvement over an nRMSE of 15.85%, based on the uncorrected UAS measurements. This demonstrated the accuracy of the downwelling irradiance correction method. The spectral shape of the corrected UAS irradiance agreed well with the ground-measured irradiance, with slight deviations in the region of 400 nm to 600 nm. The same pattern of deviation was also visible in the uncorrected UAS irradiance, which shows that this deviation was not caused by the correction algorithm, but is a characteristic of the ILS sensor.

Others have chosen a similar ILS correction based on the cosine approach but estimating the diffuse and direct fractions developing a sensor approach, instead of a data-driven approach like ours. For example, Long et al. (2010) achieved an error of less than 10 W·m^{-2} for 90% of measured data points on the tilt-corrected irradiance data for their method. They used a specially designed ILS, consisting of seven separate sensors and a shading plate, which ensured that one sensor is always exposed to direct radiation, while another sensor is completely shaded from direct radiation to extract the direct and diffuse radiation contributions with a similar purpose as our endmember approach. The correction method by Suomalainen et al. (2018) resulted in stability and linearity of 2.5% during a flight. In their approach, in addition to the spectral ILS sensor, three RGB diodes were used, with SVA offsets of 10° to the ILS in order to estimate the irradiance distribution over the hemisphere. Implementation of these methods is less operational and more expensive compared to our proposed methods as they require custom engineered sensors, whereas our method only relies on readily available sensors.

One of the most remarkable aspects of our study is the possibility of acquiring images under passing clouds as this is always a large constraint when planning campaigns. Our method to correct irradiance in such a situation normalizes the reflectance-factor according to the continuous measurements each time. Moreover, our correction method is capable to account for flight instability during both high and low irradiance situations. During sections of the flight where a cloud is in the direct pathway between the sun and ILS, the calculated diffuse radiation fraction is high. In turn, the calculated diffuse radiation fraction is low when the ILS is exposed to direct sunlight and the measured downwelling irradiance is high. During periods dominated by diffuse radiation, the effect of correction is small while during periods dominated by direct radiation the correction has a strong effect. In some instances, images acquired by UAS are half-shaded and need to be discarded in further processing. Also, images where the illumination is different at the UAS compared to the image footprint, due to the solar angle, need to be filtered out.

Our study also showed that if the irradiance measurements are not properly corrected for attitude changes due to flight direction, the error propagates into the land surface reflectance-factor resulting in stripping effects co-varying with flight directions and/or wind gusts. Mapping land surface reflectance-factor without correcting the downwelling irradiance for tilt leads to obvious illumination changes in the mapped reflectance-factor unrelated to the actual land surface reflectance-factor.

In contrast, mapping the land surface reflectance-factor based on the tilt-corrected downwelling irradiance data reduces those effects greatly.

7. Conclusion

This study contributes to advance hyperspectral remote sensing from UAS by correcting for intermittent or passing clouds during the flight and for the turbulence effects typical of the lower part of the atmospheric boundary layer during daytime. We also characterized and calibrated the hyperspectral camera precisely, which allows for better planning of flight operations and to implement data processing algorithms, tuned to the actual sensor's capabilities.

A radiometric accuracy of the CUBERT sensor of 6% was obtained and it was found that the actual dynamic range of the sensor was lower than the reported one. This information was key to adjust the exposure in field campaigns to avoid DN above 1800, to adjust to the actual dynamic range. The spectral calibration indicates that the CUBERT sensor can be used as a hyperspectral imager in the visible range and red edge, but above around 800 nm, the application of narrowband indices or the detection of narrow spectral absorption features will be truly compromised.

The proposed method of unmixing downwelling irradiance was able to correct for variations due to platform tilting under clear sky conditions and intermittent clouds. The variability of downwelling irradiance was reduced to 3% (a reduction of 81%) for systematic shifts and by up to 74% for high-frequency variations, which consequently reduced surface reflectance-factor stripping effects. The achieved accuracy of broadband downwelling irradiance was an nRMSE of 2.78%, compared to ground-based measurements. The method, with similar performance to more expensive and technically complex sensor based methods, could be applied to a wide variety of ILS sensors and UAS platforms, making UAS missions more similar to airborne or satellite missions in terms of stability.

Being able to retrieve accurate hyperspectral reflectance-factor under clouds increases the timeframe during which data can be collected, without the revisit intervals being determined by weather conditions. Moreover, the majority of the algorithms applied with hyperspectral UAS datasets, have been borrowed from satellite remote sensing and tend to be biased towards clear sky conditions. Accurate UAS datasets acquired at high spatial resolution can open up the possibility for studying new questions related to fluctuating light environments on photosynthesis and radiative transfer on plant canopies or to upscale between field and hyperspectral satellite missions and fill the gaps during cloudy conditions.

Supplementary data to this article can be found online at https://doi.org/10.1016/j.rse.2021.112719.

Declaration of Competing Interest

The authors declare that they have no known competing financial interests or personal relationships that could have appeared to influence the work reported in this paper.

team at HIDROCEC, Universidad Nacional, Liberia, Costa Rica for their support in the field.

References

Aasen, H., Bolten, A., 2018. Multi-temporal high-resolution imaging spectroscopy with hyperspectral 2D imagers – from theory to application. Remote Sens. Environ. 205, 374–389. https://doi.org/10.1016/j.rse.2017.10.043.

Aasen, H., Bendig, J., Bolten, A., Bennertz, S., Willkomm, M., Bareth, G., 2014. Introduction and preliminary results of a calibration for full-frame hyperspectral cameras to monitor agricultural crops with UAVs. ISPRS - Int. Arch. Photogramm. Remote Sens. Spat. Inf. Sci. XL–7, 1–8. https://doi.org/10.5194/isprsarchives-XL-7-1-2014.

Aasen, H., Honkavaara, E., Lucieer, A., Zarco-Tejada, P., 2018. Quantitative remote sensing at ultra-high resolution with UAV spectroscopy: a review of sensor technology, measurement procedures, and data correction workflows. Remote Sens. 10, 1091. https://doi.org/10.3390/rs10071091.

Boers, R., Mitchell, R.M., Krummel, P.B., 1998. Correction of aircraft pyranometer measurements for diffuse radiance and alignment errors. J. Geophys. Res. Atmos. 103, 16753–16758. https://doi.org/10.1029/98JD01431.

Brachmann, J.F.S., Baumgartner, A., Lenhard, K., 2016. Calibration procedures for imaging spectrometers: improving data quality from satellite missions to UAV campaigns. In: Meynart, R., Neeck, S.P., Kimura, T., Shimoda, H. (Eds.), Sensors, Systems, and Next-Generation Satellites XX. https://doi.org/10.1117/12.2240076, p. 1000010.

Burkart, A., Cogliati, S., Schickling, A., Rascher, U., 2014. A novel UAV-based ultra-light weight spectrometer for field spectroscopy. IEEE Sensors J. 14, 62–67. https://doi.org/10.1109/JSEN.2013.2279720.

Cao, J., Leng, W., Liu, K., Liu, L., He, Z., Zhu, Y., 2018. Object-Based mangrove species classification using unmanned aerial vehicle hyperspectral images and digital surface models. Remote Sens. 10 https://doi.org/10.3390/rs10010089.

Coppo, P., Brandani, F., Faraci, M., Sarti, F., Dami, M., Chiarantini, L., Ponticelli, B., Giunti, L., Fossati, E., Cosi, M., 2020. Leonardo spaceborne infrared payloads for Earth observation: SLSTRs for Copernicus Sentinel 3 and PRISMA hyperspectral camera for PRISMA satellite. Appl. Opt. 59, 6888. https://doi.org/10.1364/AO.389485.

Finnigan, J.J., Shaw, R.H., Patton, E.G., 2009. Turbulence structure above a vegetation canopy. J. Fluid Mech. 637, 387–424. https://doi.org/10.1017/S0022112009990589.

Glennie, C., 2008. Rigorous 3D error analysis of kinematic scanning LIDAR systems. J. Appl. Geod. 1, 147–157. https://doi.org/10.1515/jag.2007.017.

Guanter, L., Segl, K., Kaufmann, H., 2009. Simulation of optical remote-sensing scenes with application to the EnMAP hyperspectral mission. IEEE Trans. Geosci. Remote Sens. 47, 2340–2351. https://doi.org/10.1109/TGRS.2008.2011616.

Hakala, T., Markelin, L., Honkavaara, E., Scott, B., Theocharous, T., Nevalainen, O., Näsi, R., Suomalainen, J., Viljanen, N., Greenwell, C., Fox, N., 2018. Direct reflectance measurements from drones: sensor absolute radiometric calibration and system tests for forest reflectance characterization. Sensors (Switzerland) 18. https://doi.org/10.3390/s18051417.

Honkavaara, E., Näsi, R., Oliveira, R., Viljanen, N., Suomalainen, J., Khoramshahi, E., Hakala, T., Nevalainen, O., Markelin, L., Vuorinen, M., Kankaanhuhta, V., Lyytikäinen-Saarenmaa, P., Haataja, L., 2020. Using multitemporal hyper-and multispectral UAV imaging for detecting bark beetle infestation on norway spruce. Int. Arch. Photogramm. Remote Sens. Spat. Inf. Sci. - ISPRS Arch. 43, 429–434. https://doi.org/10.5194/isprs-archives-XLIII-B3-2020-429-2020.

Huang, J., Sun, Y., Wang, M., Zhang, D., Sada, R., Li, M., 2017. Juvenile tree classification based on hyperspectral image acquired from an unmanned aerial vehicle. Int. J. Remote Sens. 38, 2273–2295. https://doi.org/10.1080/01431161.2016.1219076.

Ishihara, M., Inoue, Y., Ono, K., Shimizu, M., Matsuura, S., 2015. The impact of sunlight conditions on the consistency of vegetation indices in croplands—effective usage of vegetation indices from continuous ground-based spectral measurements. Remote Sens. 7, 14079–14098. https://doi.org/10.3390/rs71014079.

Lee, C.M., Cable, M.L., Hook, S.J., Green, R.O., Ustin, S.L., Mandl, D.J., Middleton, E.M., 2015. An introduction to the NASA Hyperspectral InfraRed Imager (HyspIRI) mission and preparatory activities. Remote Sens. Environ. 167, 6–19. https://doi.org/10.1016/j.rse.2015.06.012.

Liu, H., Zhu, H., Wang, P., 2017. Quantitative modelling for leaf nitrogen content of winter wheat using UAV-based hyperspectral data. Int. J. Remote Sens. 38, 2117–2134. https://doi.org/10.1080/01431161.2016.1253899.

Long, C.N., Bucholtz, A., Jonsson, H., Schmid, B., Vogelmann, A., Wood, J., 2010. A method of correcting for tilt from horizontal in downwelling shortwave irradiance measurements on moving platforms. Open Atmos. Sci. J. 4, 78–87. https://doi.org/10.2174/1874282301004010078.

Lucieer, A., Malenovský, Z., Veness, T., Wallace, L., 2014. HyperUAS-imaging spectroscopy from a multirotor unmanned aircraft system. J. F. Robot. 31, 571–590. https://doi.org/10.1002/rob.21508.

Manfreda, S., McCabe, M., Miller, P., Lucas, R., Pajuelo Madrigal, V., Mallinis, G., Ben Dor, E., Helman, D., Estes, L., Ciraolo, G., Müllerová, J., Tauro, F., de Lima, M., de Lima, J., Maltese, A., Frances, F., Caylor, K., Kohv, M., Perks, M., Ruiz-Pérez, G., Su, Z., Vico, G., Toth, B., 2018. On the use of unmanned aerial systems for environmental monitoring. Remote Sens. 10, 641. https://doi.org/10.3390/rs10040641.

Pharr, M., Jakob, W., Humphreys, G., 2017. Color and Radiometry, in: Physically Based Rendering. Elsevier, pp. 313–353. https://doi.org/10.1016/B978-0-12-800645-0.50005-1.

Reda, I., Andreas, A., 2004. Solar position algorithm for solar radiation applications. Sol. Energy 76, 577–589. https://doi.org/10.1016/j.solener.2003.12.003.

Schaepman-Strub, G., Schaepman, M.E., Painter, T.H., Dangel, S., Martonchik, J.V., 2006. Reflectance quantities in optical remote sensing-definitions and case studies. Remote Sens. Environ. 103, 27–42. https://doi.org/10.1016/j.rse.2006.03.002.

Suomalainen, J., Hakala, T., de Oliveira, R.A., Markelin, L., Viljanen, N., Näsi, R., Honkavaara, E., 2018. A novel tilt correction technique for irradiance sensors and spectrometers on-board unmanned aerial vehicles. Remote Sens. 10, 1–18. https://doi.org/10.3390/rs10122068.

Suomi, I., Gryning, S.-E., Floors, R., Vihma, T., Fortelius, C., 2015. On the vertical structure of wind gusts. Q. J. R. Meteorol. Soc. 141, 1658–1670. https://doi.org/10.1002/qj.2468.

Wang, S., Baum, A., Zarco-Tejada, P.J., Dam-Hansen, C., Thorseth, A., Bauer-Gottwein, P., Bandini, F., Garcia, M., 2019a. Unmanned Aerial System multispectral mapping for low and variable solar irradiance conditions: potential of tensor decomposition. ISPRS J. Photogramm. Remote Sens. 155, 58–71. https://doi.org/10.1016/j.isprsjprs.2019.06.017.

Wang, S., Garcia, M., Ibrom, A., Bauer-Gottwein, P., 2019b. Temporal interpolation of land surface fluxes derived from remote sensing – results with an Unmanned Aerial System. Hydrol. Earth Syst. Sci. Discuss. 1–27. https://doi.org/10.5194/hess-2019-490.

Zarco-Tejada, P.J., Guillén-Climent, M.L., Hernández-Clemente, R., Catalina, A., González, M.R., Martín, P., 2013. Estimating leaf carotenoid content in vineyards using high resolution hyperspectral imagery acquired from an unmanned aerial vehicle (UAV). Agric. For. Meteorol. 171–172, 281–294. https://doi.org/10.1016/j.agrformet.2012.12.013.

Zarco-Tejada, P.J., Hornero, A., Beck, P.S.A., Kattenborn, T., Kempeneers, P., Hernández-Clemente, R., 2019. Chlorophyll content estimation in an open-canopy conifer forest with Sentinel-2A and hyperspectral imagery in the context of forest decline. Remote Sens. Environ. 223, 320–335. https://doi.org/10.1016/j.rse.2019.01.031.